Fig. 8. The seven *Planck* polarization maps from 30 to 353 GHz, shown in Stokes *Q* and *U*, and in total polarized intensity (*P*). All maps are corrected for temperature-to-polarization leakage due to bandpass mismatch. The colour scale uses the same function as in Fig. 7, but the range limits have been adjusted.

Table 6. Main characteristics of HFI full mission maps.

| Characteristic | Reference frequency ν [GHz] | | | | | | Notes |
	100	143	217	353	545	857	
Number of bolometers	8	11	12	12	3	4	$a1$
Effective beam FWHM$_1$ [arcmin]	9.68	7.30	5.02	4.94	4.83	4.64	$b1$
Effective beam FWHM$_2$ [arcmin]	9.66	7.22	4.90	4.92	4.67	4.22	$b2$
Effective beam ellipticity ϵ	1.186	1.040	1.169	1.166	1.137	1.336	$b3$
Noise per beam solid angle [μK_{CMB}]	7.5	4.3	8.7	29.7			$c1$
[kJy sr^{-1}]					9.1	8.8	$c1$
Temperature noise [μK_{CMB} deg]	1.29	0.55	0.78	2.56			$c2$
[kJy sr^{-1} deg]					0.78	0.72	$c2$
Polarization noise (Q and U) [μK_{CMB} deg]	1.96	1.17	1.75	7.31			$c3$
Calibration accuracy [%]	0.09	0.07	0.16	0.78	1.1(+5)	1.4(+5)	d
CIB monopole prediction [MJy sr^{-1}]	0.0030	0.0079	0.033	0.13	0.35	0.64	e
Zodiacal light level correction [K$_{CMB}$]	4.3×10^{-7}	9.4×10^{-7}	3.8×10^{-6}	3.4×10^{-5}			$e2$
[MJy sr^{-1}]					0.04	0.12	$e2$

Notes. $^{(a1)}$ Number of bolometers whose data were used in producing the channel map. $^{(b1)}$ FWHM$_1$ is the FWHM of the Gaussian whose solid angle is equivalent to that of the effective beams. $^{(b2)}$ FWHM$_2$ is the FWHM of the elliptical Gaussian fit. $^{(b3)}$ Ratio of the major to minor axis of the best-fit Gaussian averaged over the full sky. $^{(c1)}$ Estimate of the noise per beam solid angle, as given in $b1$. $^{(c2)}$ Estimate of the noise in intensity, scaled to 1°, assuming that the noise is white. $^{(c3)}$ Estimate of the noise in polarization, scaled to 1°, assuming that the noise is white. $^{(d)}$ Calibration accuracy (at 545 and 857 GHz, the 5% accounts for the model uncertainty). $^{(e)}$ According to the Béthermin et al. (2012) model, whose uncertainty is estimated to be at the 20% level (also for constant νI_ν). $^{(e2)}$ Zero-level correction to be applied on zodiacal-light corrected maps.

the shape of the effective beam at that location. Zero-levels are estimated by fitting a cosecant-law Galactic latitude model to the CMB-subtracted maps, and subtracting this from the maps. The polarization maps must be corrected for bandpass leakage through multiplication with leakage template maps, which are estimated via a process similar to component separation.

A summary of the characteristics of the LFI maps is presented in Table 5.

7.1.2. HFI

As for the *Planck* 2013 release, the measurements in each `HEALPix` pixel visited during a stable pointing period (i.e., "ring") are averaged for each detector, keeping track of the bolometer orientations on the sky. The calibration and mapmaking operations use this intermediate product as an input. For each detector, the TOIs are only modified by a single offset value per ring, determined using the destriping method described in Tristram et al. (2011). The offsets are computed simultaneously for all bolometers at a given frequency, using the full mission data. For a given bolometer, the same offset per ring is applied whatever the map (e.g., full-mission, half-mission, detector-set maps; but for half-ring maps, see Planck Collaboration VII 2016). Each data sample is calibrated in K_{CMB} for the 100, 143, 217, and 353 GHz channels, and MJy sr^{-1} (assuming $\nu I_\nu =$ constant) for the 545 and 857 GHz channels, using the calibration scheme presented in Sect. 5.4.2. Unlike in the 2013 release, the bolometer gains are assumed to be constant throughout the mission. The final mapmaking is a simple projection of each un-flagged sample to the nearest grid pixel. For polarization data, when several detectors are solved for simultaneously, the polarization mapmaking equation is inverted on a per-pixel basis (Planck Collaboration VII 2016).

The products of the HFI mapmaking pipelines are pixelized maps of I, Q, and U, together with their covariances. Map resolution is $N_{side} = 2048$, and the pixel size is 1′.7. The basic characteristics of the maps are given in Table 6. For details, see (Planck Collaboration VII 2016).

Maps are cleaned for the zodiacal light component, which varies in time, based on templates fitted to the survey difference maps (see Planck Collaboration XIV 2014). These templates are systematically subtracted prior to mapmaking. The *Planck* total dipole (Solar and orbital) is computed and also subtracted from the data. In contrast to 2013, the far sidelobes (FSL) are not removed from the maps.

The 2015 HFI maps delivered via the PLA have had zodiacal light removed, and include CIB emission. In addition, the zero level of the temperature maps has been adjusted for Galactic emission. However, the zero level adjustment was based on maps that contained zodiacal light, and therefore the released maps require an additional frequency-dependent correction that must be applied manually. For work requiring all astrophysical sources of emission to be present in the maps, the "Zodiacal light level correction" ("e2" in the "Notes" column of Table 6) must be added to the maps. For work requiring Galactic emission only, the "e2" corrections should be added to the maps, but the "CIB monopole prediction" ("e" in the "Notes" column) should be removed.

8. CMB products

8.1. CMB maps

As for the *Planck* 2013 release, we use four different methods to separate the *Planck* 2015 frequency maps into physical components (Planck Collaboration IX 2016). The four methods
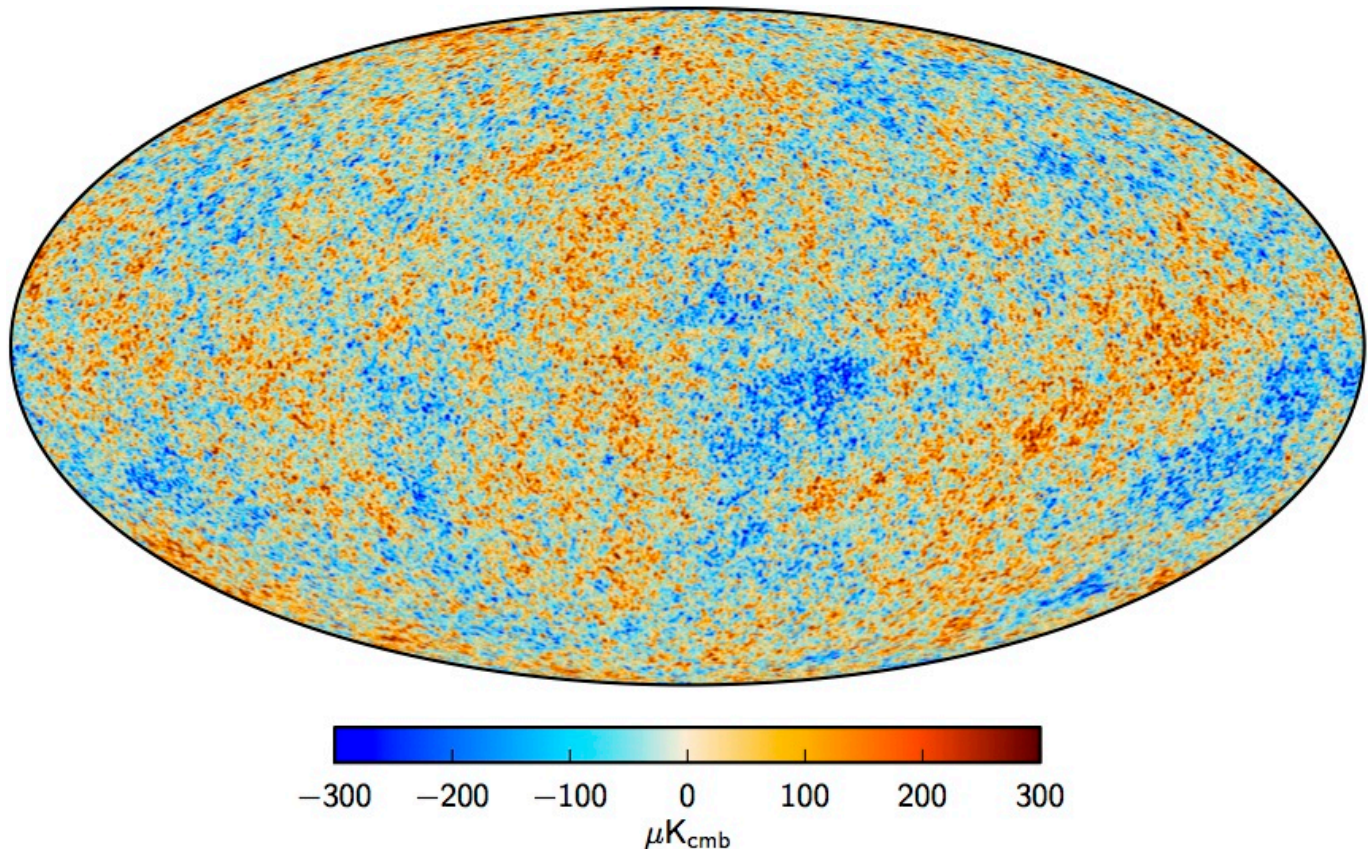
Fig. 9. Maximum posterior CMB intensity map at 5′ resolution derived from the joint baseline analysis of *Planck*, WMAP, and 408 MHz observations. A small strip of the Galactic plane, covering 1.6% of the sky, is filled in by a constrained realization that has the same statistical properties as the rest of the sky (Planck Collaboration IX 2016).

are: SMICA, which uses an independent component analysis of power spectra (Delabrouille et al. 2003; Cardoso et al. 2008); NILC, a needlet-based internal linear combination approach (Delabrouille et al. 2009); Commander, a pixel-based parameter and template fitting procedure with Gibbs sampling (Eriksen et al. 2006, 2008); and SEVEM, which employs template fitting (Fernández-Cobos et al. 2012). The methods used are conceptually the same as in 2013, but we now apply them independently to the temperature and polarization maps. Similarly to what was done in 2013, simulations (in this case FFP8, Planck Collaboration XII 2016) are used to test the methods and estimate uncertainties in the recovery of components.

All four methods produce CMB maps in Stokes I, Q, and U. In addition, Commander and SMICA separate diffuse astrophysical "foregrounds" characterized by their different spectral signatures. Commander does so by fitting physical models of these foregrounds and the CMB to the sky, whereas SMICA extracts a fixed set of independent components representing CMB, foregrounds, and noise. Typically, SMICA assumes that two "foregrounds" are present at low and high frequencies, respectively. An important change in the implementation of Commander in 2015 is in the input maps used, which now include detector-level maps rather than maps that combine all detectors at a given frequency, a map of 408 MHz emission, and the 9 yr WMAP maps. The significant increase in the number of input maps allows Commander to control much better several factors, such as relative calibration and the frequency response of individual channels, and to extract a larger number of foreground temperature

components, now matching those that are expected to be present in the sky.

The 2015 *Planck* CMB temperature maps produced by all four methods (see an example in Fig. 9) have significantly lower noise than those produced in 2013 (by a factor of 1.3). They are used mainly for non-Gaussianity analysis (Planck Collaboration XVII 2016; Planck Collaboration XVI 2016) and for the extraction of lensing deflection maps (Planck Collaboration XV 2016). For these analyses, all four methods are considered to give equivalently robust results, and the dispersion between the four gives a reasonable estimate of the uncertainty of the CMB recovery. We emphasize, however, that these maps are not cleaned of high-ℓ foregrounds, such as unresolved extragalactic sources, or of SZ emission. Although the strongest compact sources are removed through a masking procedure based on optimal filters such as Mexican Hat wavelets, unresolved sources escaping this process introduce small-scale power beyond $\ell \approx 2000$, which if uncorrected will bias cosmological parameters. Cosmological analyses using small angular scales must therefore take care to marginalize over such foregrounds as appropriate (see Planck Collaboration IX 2016 and Planck Collaboration XIII 2016).

Although the statistical properties of these maps give good results when used to fit cosmological models, the best *Planck* 2015 cosmological parameters are derived from a likelihood code that allows more detailed tuning of the contribution of individual frequencies and ℓ-by-ℓ removal of foregrounds (Planck Collaboration XIII 2016).
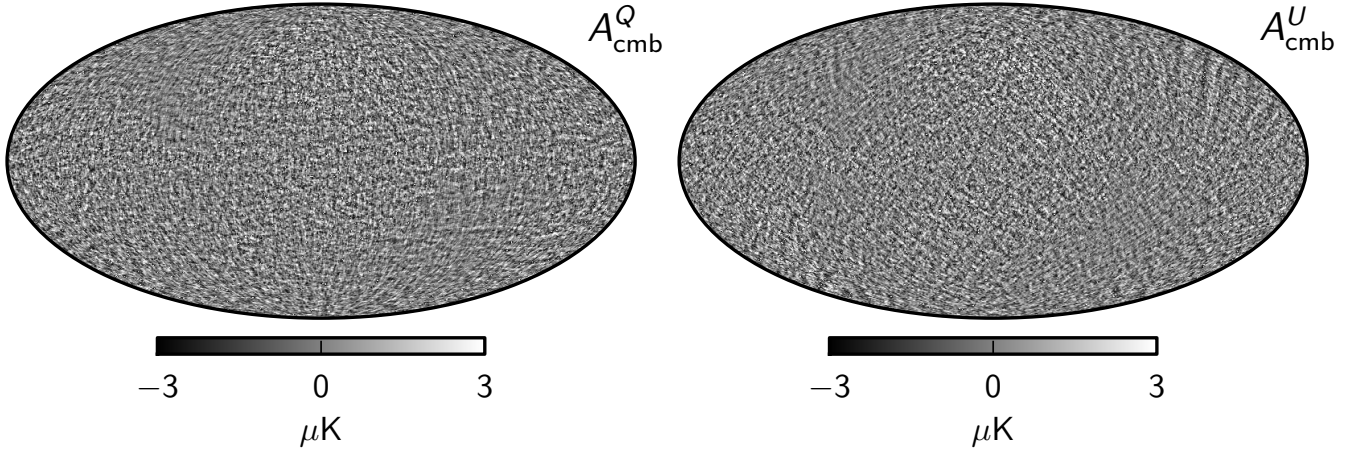
Fig. 10. Maximum posterior amplitude Stokes *Q* (*left*) and *U* (*right*) maps derived from *Planck* observations between 30 and 353 GHz. These maps have been highpass-filtered with a cosine-apodized filter between $\ell = 20$ and 40, and a 17% region of the Galactic plane has been replaced with a constrained Gaussian realization (Planck Collaboration IX 2016). From Planck Collaboration X (2016).

A low-resolution version of the `Commander` map is also used in the pixel-based low-ℓ likelihood component of our best-fit 2015 cosmology (Planck Collaboration XI 2016).

In polarization, the CMB maps resulting from the 2015 *Planck* component-separation methods represent a dramatic advance in terms of coverage, angular resolution, and sensitivity. Nonetheless, they suffer from a significant level of anomalous features at large angular scales, arising from corresponding systematic effects in the input frequency maps between 100 and 217 GHz. The characterization of these systematic effects is ongoing, and it is currently suspected that low-level spurious signals are also present at intermediate angular scales (Planck Collaboration VII 2016; Planck Collaboration VIII 2016). For this reason, the CMB polarization maps presented here have been highpass-filtered with a cosine-apodized filter between $\ell = 20$ and 40 (Fig. 10). They are used only for a very limited number of cosmological analyses, which have been shown to be immune to the undesired features still present: estimation of primordial non-Gaussianity levels (Planck Collaboration XVII 2016); stacking analysis (Planck Collaboration XVI 2016); estimation of primordial magnetic field levels (Planck Collaboration XIX 2016); and estimation of lensing potential (Planck Collaboration XV 2016).

In contrast, the low-ℓ polarization likelihood used in Planck Collaboration XIII (2016) is based exclusively on the 70 GHz polarization map, cleaned of foregrounds by use of the 30 and 353 GHz polarization maps. Both of these frequencies have been shown to be free of the kind of systematic errors that still affect intermediate frequencies (Planck Collaboration II 2016; Planck Collaboration VIII 2016).

8.2. CMB power spectra

The foreground-subtracted, frequency-averaged, cross-half-mission *TT* spectrum is plotted in Fig. 11, together with the `Commander` power spectrum at multipoles $\ell < 29$. The figure also shows the best-fit base ΛCDM theoretical spectrum fitted to the PlanckTT+lowP likelihood, together with residuals (bottom panel) and $\pm 1\sigma$ uncertainties. Note that we use the notation "PlanckTT" when we are referring to the likelihood deriving from the *TT* spectrum, and so on.

8.2.1. Polarization power spectra

In addition to the *TT* spectra, the 2015 *Planck* likelihood includes the *TE* and *EE* spectra, shown in Fig. 12. The theory curve in Fig. 12 is the best-fit base ΛCDM model fitted to the temperature spectra using the PlanckTT+lowP likelihood. The residuals are higher than expected from noise alone, and provide evidence of residual systematic errors in the *TE* and *EE* spectra. It is currently believed that the dominant source of such errors is beam mismatch generating leakage from temperature to polarization at the level of a few μK^2 in $\mathcal{D}_\ell$. We urge caution in the interpretation of any features in these spectra, which should be viewed as work in progress. Nonetheless, we find a high level of consistency in results between the PlanckTT and the full TT+TE+EE likelihoods. Furthermore, the cosmological parameters (which do not depend strongly on τ) derived from the *TE* spectra have comparable errors to the *TT*-derived parameters, and they are consistent typically within 0.5σ or better.

8.2.2. Number of modes

One way of assessing the constraining power contained in a particular measurement of CMB anisotropies is to determine the effective number of $a_{\ell m}$ modes that have been measured. This is equivalent to estimating 2 times the square of the total S/N in the power spectra, a measure that contains *all* the available cosmological information if we assume that the anisotropies are purely Gaussian (and hence ignore all non-Gaussian information coming from lensing, the CIB, cross-correlations with other probes, etc.). Carrying out this procedure for the *Planck* 2013 *TT* power spectrum data provided in Planck Collaboration XV (2014) and Planck Collaboration XVI (2014) yields the number 826 000 (which includes the effects of instrumental noise, cosmic variance, and masking). The 2015 *TT* data have increased this value to 1 114 000, with *TE* and *EE* adding a further 60 000 and 96 000 modes, respectively[6]. From this perspective the 2015 *Planck* data constrain approximately 55% more modes than in the 2013 release. Of course this is not the whole story, since some pieces of information are more valuable than others, and in fact *Planck* is able to place considerably tighter constraints on

---

[6] Here we have used the basic (and conservative) likelihood; more modes are effectively probed by *Planck* if one includes larger sky fractions.
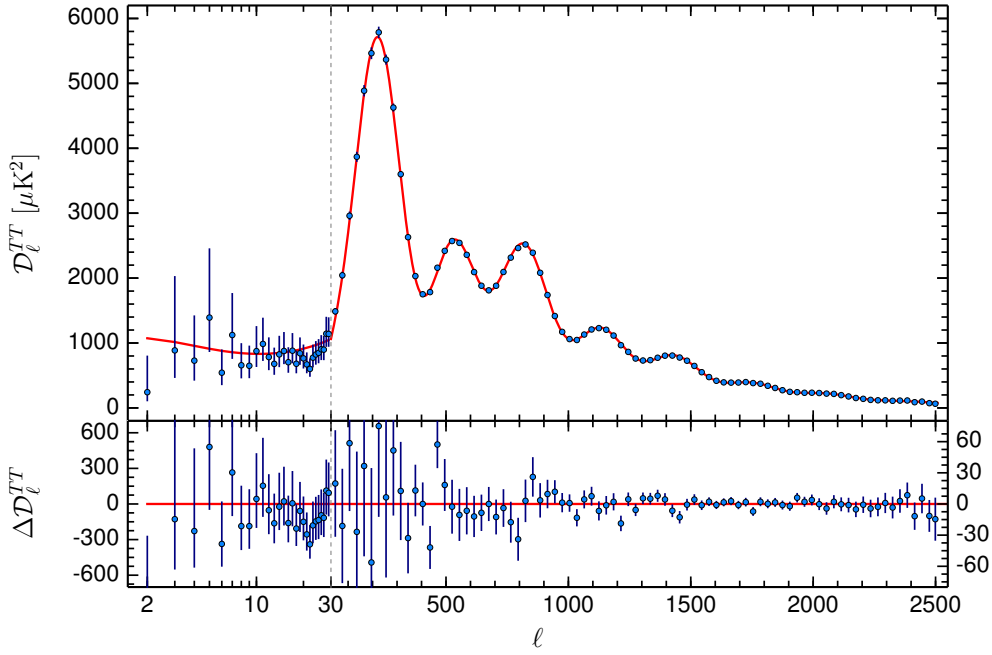
Fig. 11. *Planck* 2015 temperature power spectrum. At multipoles $\ell \geq 30$, we show the maximum-likelihood, frequency-averaged temperature spectrum computed from the cross-half-mission likelihood, with foreground and other nuisance parameters determined from the MCMC analysis of the base ΛCDM cosmology. In the multipole range $2 \leq \ell \leq 29$, we plot the power spectrum from the `Commander` component-separation algorithm computed over 94% of the sky. The best-fit base ΛCDM theoretical spectrum fitted to the PlanckTT+lowP likelihood is plotted in the *upper panel*. Residuals with respect to this model are shown in the *lower panel*. The error bars show $\pm 1\sigma$ uncertainties. From Planck Collaboration XIII (2016).

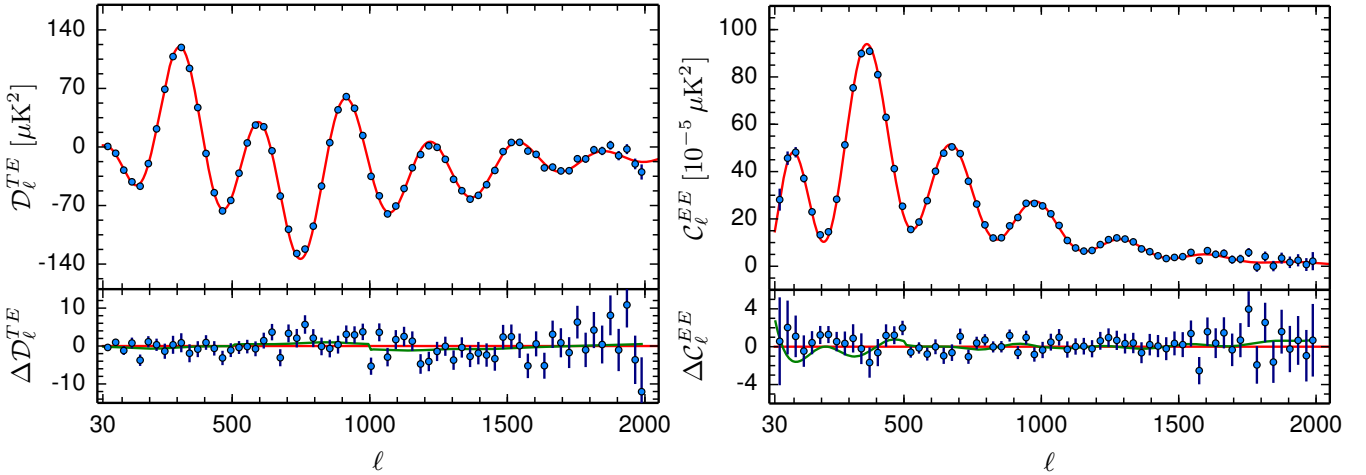**Fig. 12.** Frequency-averaged TE (*left*) and EE (*right*) spectra, not corrected for T-to-P leakage (see text). The theoretical TE and EE spectra plotted in the *upper panels* are computed from the best-fit model of Fig. 11. Residuals with respect to this theoretical model are shown in the *lower panels*. The error bars show $\pm 1\sigma$ uncertainties. The green lines in the lower panels show the best-fit temperature-to-polarization leakage model, fitted separately to the TE and EE spectra. From Planck Collaboration XIII (2016).

particular parameters (e.g., reionization optical depth or certain extensions to the base ΛCDM model) by including new polarization data.

8.2.3. Peaks in the power spectra

The fidelity with which *Planck* has measured the C_ℓ^{TT}, C_ℓ^{TE}, and C_ℓ^{EE} power spectra enables us to estimate precisely the underlying cosmological parameters (see Sect. 10), but the C_ℓs are themselves a set of cosmological observables, whose properties can be described independently of any model. The acoustic peaks in the C_ℓs reveal the underlying physics of oscillating sound

waves in the coupled photon-baryon fluid, driven by dark matter potential perturbations, and one can talk about the fundamental mode, the first harmonic, and so on. Hence it is natural to ask about the positions of the individual peaks in the power spectra as empirical information that becomes part of the canon of facts now known about our Universe.

Here we use the *Planck* data directly to fit for the multipoles of individual features in the measured TT, TE, and EE power spectra. We specifically use the CMB-only bandpowers given in Planck Collaboration XI (2016), adopting the same weighting scheme within each bin. Fitting for the positions and amplitudes of features in the bandpowers is a topic with a long history, with approaches becoming more sophisticated as the fidelity of the

Table 7. *Planck* power spectra peak positions and amplitudes.

Number	Position [ℓ]	Amplitude [μK^2]
TT power spectrum		
First	220.0 ± 0.5	5717 ± 35
Second	537.5 ± 0.7	2582 ± 11
Third	810.8 ± 0.7	2523 ± 10
Fourth	1120.9 ± 1.0	1237 ± 4
Fifth	1444.2 ± 1.1	797.1 ± 3.1
Sixth	1776 ± 5	377.4 ± 2.9
Seventh	2081 ± 25	214 ± 4
Eighth	2395 ± 24	105 ± 4
TE power spectrum		
First	308.5 ± 0.4	115.9 ± 1.1
Second	595.3 ± 0.7	28.6 ± 1.1
Third	916.9 ± 0.5	58.4 ± 1.0
Fourth	1224 ± 1.0	0.7 ± 0.5
Fifth	1536 ± 2.8	5.6 ± 1.3
Sixth	1861 ± 4	1.2 ± 1.0
EE power spectrum		
First	137 ± 6	1.15 ± 0.07
Second	397.2 ± 0.5	22.04 ± 0.14
Third	690.8 ± 0.6	37.35 ± 0.25
Fourth	992.1 ± 1.3	41.8 ± 0.5
Fifth	1296 ± 4	31.6 ± 1.0

data has improved (e.g., Scott & White 1994; Hancock & Rocha 1997; Knox & Page 2000; de Bernardis et al. 2002; Bond et al. 2003; Page et al. 2003; Durrer et al. 2003; Readhead et al. 2004; Jones et al. 2006; Hinshaw et al. 2007; Corasaniti & Melchiorri 2008; Pryke et al. 2009). Following earlier approaches, we fit Gaussians to the peaks in C_ℓ^{TT} and C_ℓ^{EE}, but parabolas to the peaks in C_ℓ^{TE}. We have to remove a featureless damping tail to fit the higher C_ℓ^{TT} region, and care has to be taken to treat the lowest-ℓ "recombination" peak in C_ℓ^{EE}. We explicitly focus on peaks (ignoring the troughs) in the conventional quantity $\mathcal{D}_\ell \equiv \ell(\ell+1)C_\ell/2\pi$; note that other quantities (e.g., C_ℓ) will have maxima at slightly different multipoles, and that the choice of bandpowers to use for fitting each peak is somewhat subjective. Our numerical values, presented in in Table 7, are consistent with previous estimates, but with a dramatically increased number of peaks measured. *Planck* detects 19 peaks (including marginal detection of the eighth C_ℓ^{TT} peak), and an essentially equivalent number of troughs.

8.3. CMB lensing products

Planck is the first experiment with the sky coverage, angular resolution, and sensitivity to form a full-sky reconstruction of the projected mass, along every line of sight back to the surface of last scattering. Figure 13 shows the 2015 *Planck* lensing map (Planck Collaboration XV 2016), which uses as input the CMB maps produced by the SMICA code. The map combines five possible quadratic estimators based on the various correlations of the CMB temperature (*T*) and polarization (*E* and *B*).

8.4. Likelihood code

8.4.1. CMB likelihood

We adopt the same general methodology for the 2015 likelihood as in 2013, extended to include *Planck* polarization data. The likelihood is a hybrid combination of a low-multipole pixel-based likelihood with a high-multipole likelihood constructed from cross-spectra (see Planck Collaboration XI 2016 for details).

At low multipoles we now use *Planck* instead of WMAP for polarization information. The 70 GHz LFI polarization maps are cleaned with the LFI 30 GHz and HFI 353 GHz maps to mitigate foreground contamination. Based on null tests, these cleaned polarization maps are then used over 46% of the sky to construct the low-multipole likelihood (referred to as "lowP"). The Commander temperature solution, constructed from all *Planck* frequency maps, together with the Haslam 408 MHz and WMAP maps, is used over 93% of the sky. The temperature and polarization data are then treated in a unified, low-resolution, pixel-based manner for the multipole range $2 \le \ell \le 29$.

The high-ℓ likelihood uses pseudo-C_ℓ cross-spectra from HFI 100, 143, and 217 GHz maps in a "fiducial Gaussian" approximation, employing analytic covariance matrices calculated for a fiducial cosmological model. Unresolved foregrounds are modelled parametrically using power spectrum templates, with only minor changes to the model adopted in the 2013 analysis. To reduce any possible biases from co-temporal systematics, the baseline high-multipole likelihood uses cross-spectra between frequency maps constructed from the first and second halves of the full mission data. We also make more aggressive use of sky at all frequencies in the 2015 analysis. The most significant change is the addition of the option to include the *TE* and *EE* power spectra and the associated covariance matrices into the scheme, to form a combined *TT*, *TE*, *EE* likelihood at high multipoles (referred to as PlanckTT,TE,EE). Although we find firm evidence for systematics associated with temperature-to-polarization leakage in the *TE* and *EE* spectra, these systematics are at low levels. We find a high degree of consistency between the *TT*, *TE*, and *EE* spectra for the cosmological models analysed in the 2015 *Planck* papers; however, in this data release, we regard the combined *TT*, *TE*, and *EE Planck* results as preliminary and hence recommend the *TT* likelihood as the baseline.

8.4.2. Lensing likelihood

Our power spectrum measurement constrains the lensing potential power spectrum to a precision of ±2.5%, corresponding to a 1.2% constraint on the overall amplitude of matter fluctuations (σ_8), a measurement with considerable power for constraining cosmology. We have constructed two Gaussian bandpower likelihoods based on the lensing power spectrum measurement, plotted in Fig. 20. The first likelihood uses a conservative bandpower range, $40 \le L \le 400$, with linear binning, following the temperature-only likelihood released in 2013. The second likelihood uses a more aggressive range with $8 \le L \le 2048$, and bins that are linear in $L^{0.6}$. Both likelihoods combine temperature and polarization data. We incorporate uncertainties in the estimator normalization and bias corrections directly into the likelihood, using pre-calculated derivatives of these terms with respect to the CMB temperature and polarization power spectra. The construction of the lensing likelihood is described in Planck Collaboration XV (2016), and its cosmological implications are discussed in detail in Planck Collaboration XIII (2016).
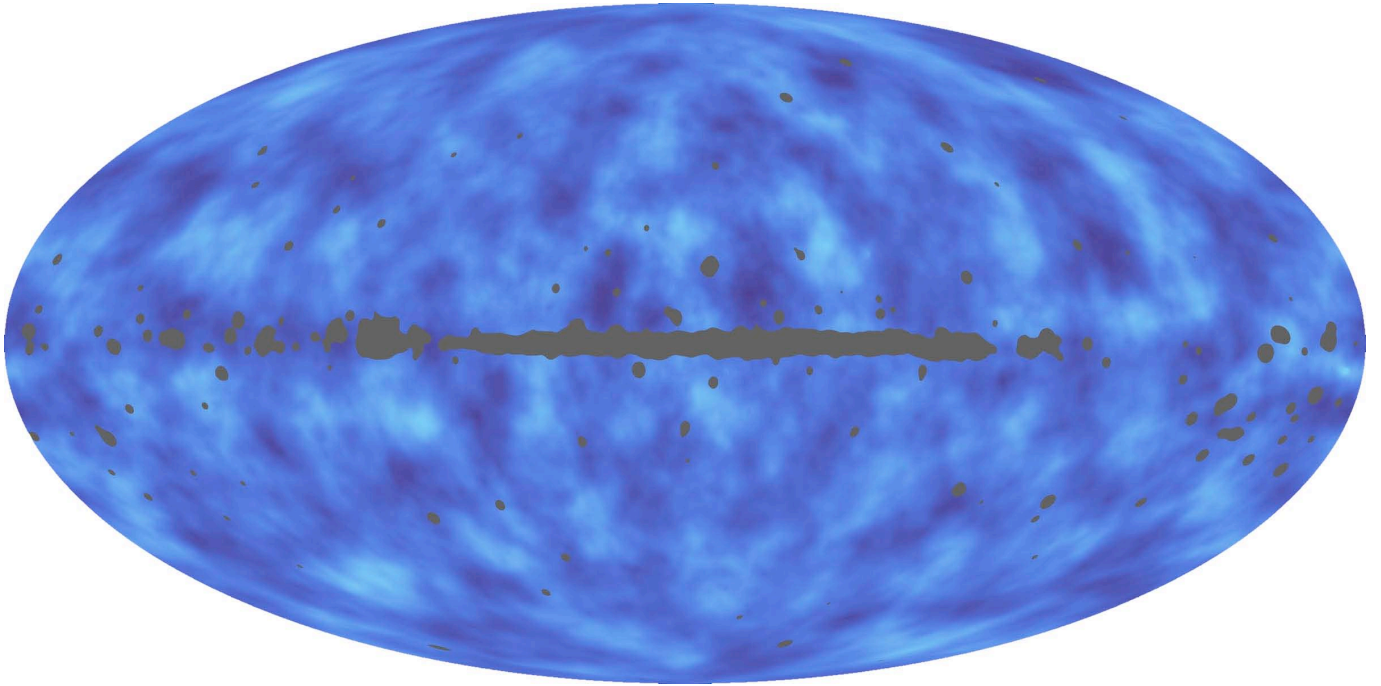
Fig. 13. Wiener-filtered lensing potential estimate with minimal masking (using the `SMICA` component-separated map), in Mollweide projection in Galactic coordinates (Planck Collaboration XV 2016). The reconstruction has been band-limited to $8 \leq L \leq 2048$ (where, following convention, L is used as the multipole index in the lensing power spectrum).

9. Astrophysics products

9.1. The Second Planck Catalogue of Compact Sources

The Second Planck Catalogue of Compact Sources (PCCS2; Planck Collaboration XXVI 2016) is the catalogue of sources detected from the full duration of *Planck* operations, referred to as the "extended" mission. It comprises compact Galactic and extragalactic sources detected over the entire sky. Compact sources are detected in the single-frequency maps and assigned to one of two sub-catalogues, the PCCS2 or PCCS2E. The first of these allows the user to produce additional sub-catalogues at higher reliability than the target 80% reliability of the full catalogue. The second contains sources whose reliability cannot be estimated, because they are embedded in a bright and complex (e.g., filamentary) background of emission.

The number of sources in the catalogue ranges from 1560 at 30 GHz up to 48 181 sources at 857 GHz. Both sub-catalogues include polarization measurements, in the form of polarized flux densities and orientation angles (or upper-limits) for all seven polarization-sensitive *Planck* channels. The number of sources with polarization information (other than upper-limits) in the catalogue ranges from 113 at 30 GHz up to 666 at 353 GHz. The improved data processing of the full-mission maps and their reduced instrumental noise levels allow us to increase the number of objects in the catalogue, improving its completeness at the target 80% reliability compared with previous versions, the PCCS (Planck Collaboration XXVIII 2014) and the Early Release Compact Source Catalogue (ERCSC; Planck Collaboration XIII 2011). The improvements are most pronounced for the LFI channels, due to the much larger increase in the data available. The completeness of the 857 GHz channel, however, has not increased, because a more refined reliability assessment resulted in a higher S/N threshold being applied in the selection function of this catalogue. Nevertheless the reliability of the PCCS2 catalogue at 857 GHz is higher than that of the PCCS.

9.2. The Second Planck Catalogue of Clusters

The Second Planck Catalogue of SZ Sources (PSZ2; Planck Collaboration XXVII 2016), based on the full mission data, is the largest SZ-selected sample of galaxy clusters yet produced and the deepest all-sky catalogue of galaxy clusters. It contains 1653 detections, of which 1203 are confirmed clusters with identified counterparts in external data sets, and is the first SZ-selected cluster survey containing $>10^3$ confirmed clusters. A total of 937 sources from the half-mission catalogue (PSZ1) released in 2013 are included, as well as 716 new detections. The completeness, which is provided as a product with the catalogue, is determined using simulated signal injection, validated through comparison to external data, and is shown to be consistent with semi-analytic expectations. The reliability is characterized using high-fidelity simulated observations and a machine-learning-based quality assessment, which together place a robust lower limit of 83% on the reliability. Using simulations, we find that the Y_{5R500} estimates are robust to pressure-profile variations and beam systematics; however, accurate conversion to Y_{500} requires the use of prior information on the cluster extent. Results of a multi-wavelength search for counterparts in ancillary data, which makes use of radio, microwave, infrared, optical, and X-ray data sets, and which places emphasis on the robustness of the counterpart match, are included in the catalogue. We discuss the physical properties of the new sample and identify a population of low-redshift, X-ray, under-luminous clusters revealed by SZ selection. Figure 14 shows the masses and redshifts for the 1093 PSZ2 clusters with known redshifts.
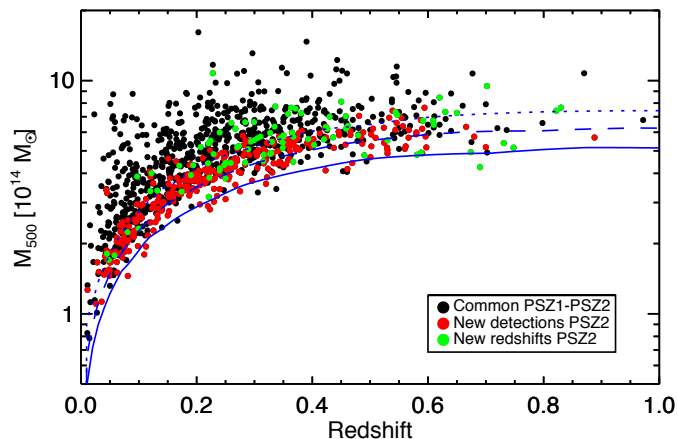
Fig. 14. M_{500}–z plane distribution of the 1093 PSZ2 clusters with known redshift. New PSZ2-detected clusters are indicated by red dots, while commmon PSZ1 and PSZ2 clusters are indicated by black dots. Green dots mark the common PSZ2–PSZ1 detections with updated redshifts in PSZ2. The solid, dashed, and dotted lines indicate the limiting mass at 20%, 50%, and 80% survey completeness, respectively.

9.3. The Planck Catalogue of Galactic Cold Clumps

The *Planck* catalogue of Galactic Cold Clumps (PGCC, Planck Collaboration XXVIII 2016) contains Galactic sources identified as cold using the CoCoCoDeT (Montier et al. 2010) multi-frequency point source detection algorithm on the *Planck* 857, 545, and 353 GHz data and the IRIS 3 THz data (Miville-Deschênes & Lagache 2005), at a resolution of 5′. This selects point sources exhibiting submillimetre excess in the 353, 545, and 857 GHz *Planck* bands simultaneously, compared to the average colour of the background, which is typical of sources appearing colder than their environment.

The PGCC catalogue is the full-mission version of the Early Cold Core (ECC) catalogue released in 2011 as part of the ERCSC (Planck Collaboration VII 2011). The ECC catalogue was built from the first 295 days of *Planck* data, and contains 915 sources selected to ensure $T < 14$ K and $S/N > 15$. A statistical description of the ECC and the extended catalogue (including sources at all temperatures and with $S/N > 4$) is given in Planck Collaboration XXII (2011), while a detailed description of a subsample of 10 sources was presented in Planck Collaboration XXIII (2011). The PGCC catalogue, included in the 2015 *Planck* release, is built on the full *Planck* mission data, and contains 13 188 Galactic sources, plus 54 sources located in the Large and Small Magellanic Clouds.

The morphology of each source is obtained using a Gaussian elliptical fit, which is then used to estimate flux densities in all bands through aperture photometry. Depending on the S/N of the flux density estimates, three categories of source are identified: 6993 sources with reliable flux densities in all bands (FLUX_QUALITY=1); 3755 sources with flux density estimates in all bands except 3 THz (FLUX_QUALITY=2), which are considered very cold candidates; and 2440 sources without reliable flux density estimates (FLUX_QUALITY=3), usually due to a complex environment, which are considered poor candidates.

Distance estimates have been obtained for 5574 PGCC sources by combining seven different methods. While PGCC sources are mainly located in the Solar neighbourhood, with 88% of sources with reliable distance estimates lying within 2 kpc of the Sun, distance estimates range from a few hundred parsecs towards local molecular clouds to 10.5 kpc towards the Galactic centre.
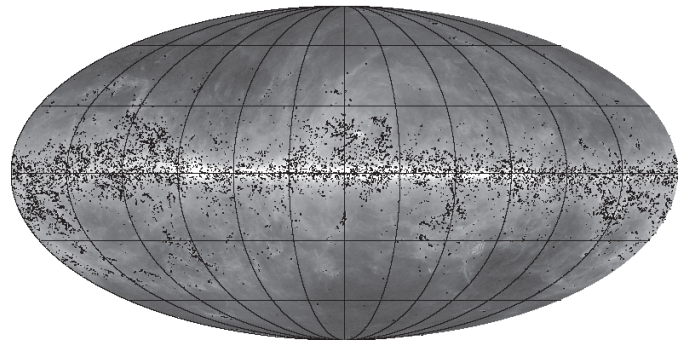

Fig. 15. All-sky distribution of the 13 188 PGCC Galactic cold clumps (black dots) and the 54 cold sources (grey dots) located in the Large and Small Magellanic Clouds. The background map is the 857 GHz *Planck* band, shown in logarithmic scale from 10^{-2} to 10^2 MJy sr^{-1}.

The temperature of each source is obtained by fitting a modified blackbody to the spectral energy density from 353 GHz to 3 THz, considering the spectral index β as a free parameter when possible. PGCC sources have an average temperature of 13–14.5 K, depending on their flux quality category, and range from 5.8 to 20 K. Other physical parameters have been derived, such as the H_2 column density, the physical size, the mass, the density, and the luminosity. It appears that the PGCC contains a large variety of objects with very different properties, from compact and dense cores to large and massive molecular clouds, located all over the sky. While a large *Herschel* programme (HKP-GCC) already followed up 315 PGCC sources with the PACS and SPIRE instruments, the PGCC catalogue is the first all-sky sample of Galactic cold sources obtained with a homogeneous method, and hence represents a gold mine for investigations of the early phases of star formation in various environments.

9.4. Diffuse Galactic foregrounds from CMB component separation

As in 2013 (Planck Collaboration X 2016), we establish a single parametric model of the microwave sky, accounting simultaneously for all significant diffuse astrophysical components and relevant instrumental effects using the Bayesian Commander analysis framework (Eriksen et al. 2004, 2006, 2008). The 2015 analysis is extended in multiple directions. First, instead of 15.5 months of temperature data, we include the full *Planck* mission data – 50 months of LFI and 29 months of HFI data – in both temperature and polarization. Second, we include the 9-year WMAP observations between 23 and 94 GHz (Bennett et al. 2013), and a 408 MHz survey map (Haslam et al. 1982), providing enough frequency constraints to decompose the low-frequency foregrounds into separate synchrotron, free-free, and spinning dust components. Third, we include the *Planck* 545 and 857 GHz frequency bands, allowing us to constrain the thermal dust temperature and emissivity index with greater precision, thereby reducing degeneracies between CMB, CO, and free-free emission. Fourth, we implement a multi-resolution technique to provide component maps at high angular resolution. Specifically, the CMB is recovered with angular resolution 5′ FWHM (Planck Collaboration IX 2016), thermal dust emission and CO $J = 2 \rightarrow 1$ lines are recovered at 7.′5 FWHM, and synchrotron, free-free, and spinning dust are recovered at 1° FWHM. Fifth, we use individual detector and detector-set maps as inputs, instead of fully-combined frequency maps. The increase in the number of input maps allows many null tests that are used to

reject individual maps exhibiting significant levels of systematic effects. Sixth, we fit for two important instrumental effects: relative calibration between detectors; and bandpass uncertainties.

The combination of these improvements allows us to reconstruct a total of six primary emission mechanisms in temperature, namely CMB, synchrotron, free-free, spinning dust, CO, and thermal dust emission, in addition to two secondary components, namely thermal SZ emission around the Coma and Virgo regions, and molecular line emission between 90 and 100 GHz. For polarization, we reconstruct three primary emission mechanisms: CMB; synchrotron; and thermal dust. All of these components are delivered as part of the 2015 *Planck* release.

Figures 16 and 17 (from Planck Collaboration X 2016) show the diffuse, high-latitude, Galactic foreground components determined from component separation in temperature and polarization. Figure 18 shows the frequency spectra of fluctuations of diffuse foreground components in temperature and polarization, compared to that of the CMB. The sky model presented in this paper provides an impressive fit to the current data, with temperature residuals at the few microkelvin level at high latitudes across the CMB-dominated frequencies, and with median fractional errors below 1% in the Galactic plane across the *Planck* frequencies. For polarization, the residuals are statistically consistent with instrumental noise at high latitudes, but limited by significant temperature-to-polarization leakage in the Galactic plane. Overall, this model represents the most accurate and complete description currently available of the astrophysical sky between 20 and 857 GHz.

9.5. Carbon monoxide emission

Carbon monoxide emission lines are present in all HFI frequency bands except 143 GHz. Using component-separation techniques, the three lowest rotational transitions can be extracted from *Planck* data, providing full-sky maps of the CO $J = 1 \rightarrow 0$, $J = 2 \rightarrow 1$, and $J = 3 \rightarrow 2$ transitions (Planck Collaboration XIII 2014). For the 2015 release, data from the full mission and better control of systematic errors lead to better maps. Table 8 summarizes the products. Figure 16 shows the `Commander` maps of all three transitions.

TYPE 1 maps are produced by a single-channel analysis, where individual bolometer maps are linearly combined to produce maps of the CO(1→0), CO(2→1), and CO(3→2) emission lines at the native resolution of the *Planck* maps. Although noisier than the other approaches, using information from a single channel strongly limits contamination from other Galactic components, such as dust or free-free emission. This makes TYPE 1 maps suitable for studying emission in the Galactic disk and CO-rich regions, but not for the high-Galactic latitudes where the CO emission is below the noise level.

TYPE 2 maps of CO(1→0) and CO(2→1) are produced using multi-channel information (i.e., using linear combinations of *Planck* channel maps smoothed to 15′). Using frequency maps, these types of product have a higher signal-to-noise ratio, allowing for their use in fainter high-Galactic latitude regions. They are, however, more susceptible to dust contamination, especially for CO(2→1), which makes them less suitable in the Galactic plane than TYPE 1 maps.

A high-resolution TYPE 3 map, as defined in Planck Collaboration XIII (2014), is not being delivered in the 2015 data release. Alternatively, another set of CO maps has been produced as part of the full `Commander` baseline multicomponent model, which is described in Planck Collaboration X (2016).

TYPE 1 and TYPE 2 maps are released with associated standard deviation maps, error maps, and masks. The suite of tests detailed in Planck Collaboration XIII (2014) has been repeated on the new TYPE 1 and TYPE 2 maps, which have been found to perform as well as their 2013 counterparts, even though small variations ($\lesssim$ 2–5 K km s^{-1}) exist in the Galactic plane.

9.5.1. All-sky Sunyaev-Zeldovich emission

The 30 to 857 GHz frequency channel maps from the *Planck* satellite survey were used to construct an all-sky map of the thermal SZ effect Planck Collaboration XXII (2016). As discussed in Planck Collaboration XXI (2014), we apply to those maps specifically tailored component-separation algorithms, MILCA Hurier et al. (2013) and NILC Remazeilles et al. (2011), that allow us to separate the thermal SZ emission from both the foreground contamination and the CMB. An orthographic view of this Compton y-map is shown in Fig. 19. This map has been characterized in terms of noise properties and residual foreground contamination, mainly thermal dust emission at large angular scales, and CIB and extragalactic point sources at small angular scales. Blindly-detected clusters in this map are consistent with those from the PSZ2 catalogue (Planck Collaboration XXVII 2016), both in terms of cluster number and integrated flux. Furthermore, by stacking individually undetected groups and clusters of galaxies we find that the y-map is consistent with thermal SZ emission even for low S/N regions. Using foreground models derived in Planck Collaboration XXIII (2016), we are able to measure the thermal SZ angular power spectrum over 50% of the sky. We conclude that the y-map is dominated by thermal SZ signal in the multipole range $20 < \ell < 800$. Similar results are obtained from a high-order-statistic analysis. The reconstructed y-map is delivered as part of the *Planck* 2015 release. We also deliver a foreground mask (which removes known point sources and regions with strong contamination from Galactic emission), a noise variance map, the estimated power spectrum, and the weights for the NILC algorithm.

10. *Planck* 2015 cosmology results

Since their discovery, anisotropies in the CMB have contributed significantly to defining our cosmological model and measuring its key parameters. The standard model of cosmology is based upon a spatially flat, expanding Universe whose dynamics are governed by General Relativity and dominated by cold dark matter and a cosmological constant (Λ). The seeds of structure have Gaussian statistics and form an almost scale-invariant spectrum of adiabatic fluctuations. The 2015 *Planck* data remain in excellent agreement with this paradigm, and continue to tighten the constraints on deviations and reduce the uncertainties on the key cosmological parameters.

The major methodological changes in the steps going from sky maps to cosmological parameters are discussed in Planck Collaboration XI (2016) and Planck Collaboration XIII (2016). These include the use of *Planck* polarization data instead of WMAP, changes to the foreground masks to include more sky and dramatically reduce the number of point source "holes", minor changes to the foreground models, improvements to the data processing, and use of cross-half-mission likelihoods (Planck Collaboration XI 2016; Planck Collaboration XIII 2016). We find good agreement with our earlier results, with increased precision.
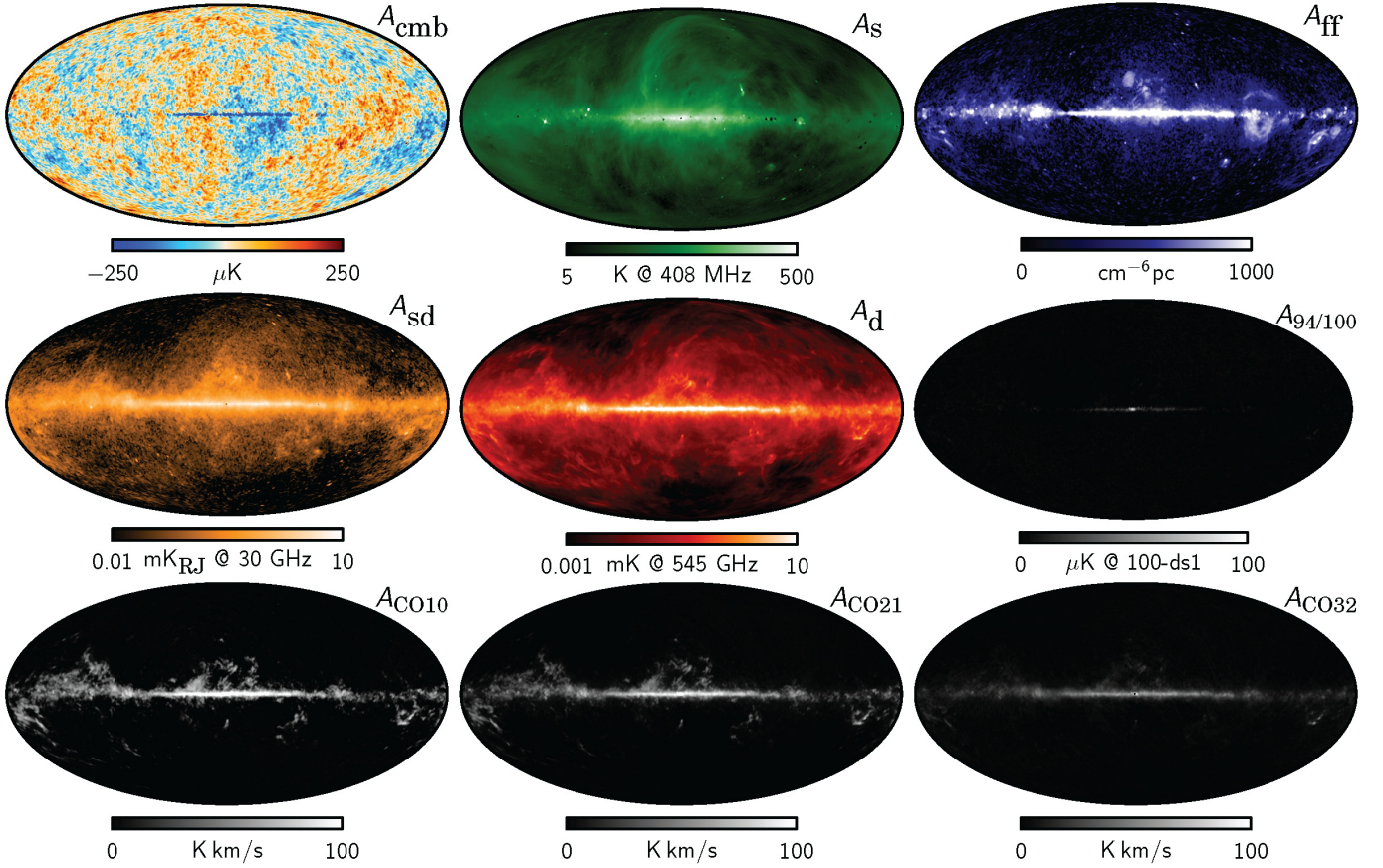
Fig. 16. Maximum posterior intensity maps derived from the joint analysis of *Planck*, WMAP, and 408 MHz observations (Planck Collaboration X 2016). *From left to right and top to bottom*: CMB; synchrotron; free-free; spinning dust; thermal dust; line emission around 90 GHz; CO $J = 1 \rightarrow 0$; CO $J = 2 \rightarrow 1$; and CO $J = 3 \rightarrow 2$.
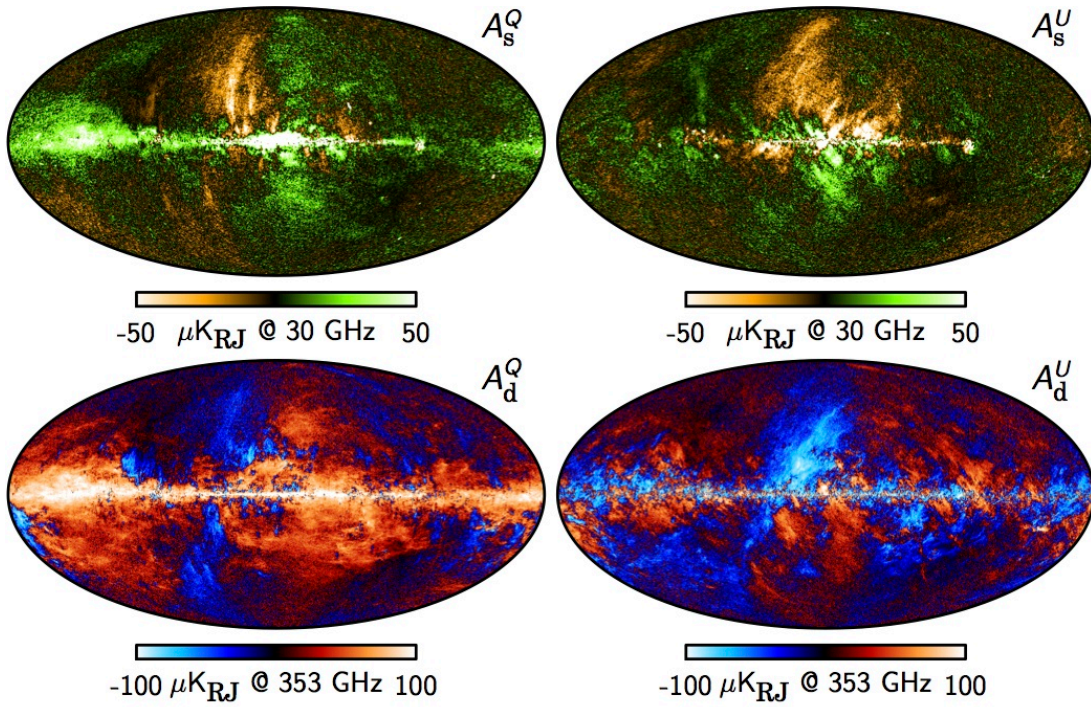

Fig. 17. Maximum posterior foreground polarization maps derived from the *Planck* observations between 30 and 353 GHz (Planck Collaboration X 2016). The *left and right columns* show Stokes Q and U parameters, respectively. *Top*: synchrotron polarization at 30 GHz. *Bottom*: thermal dust polarization at 353 GHz.
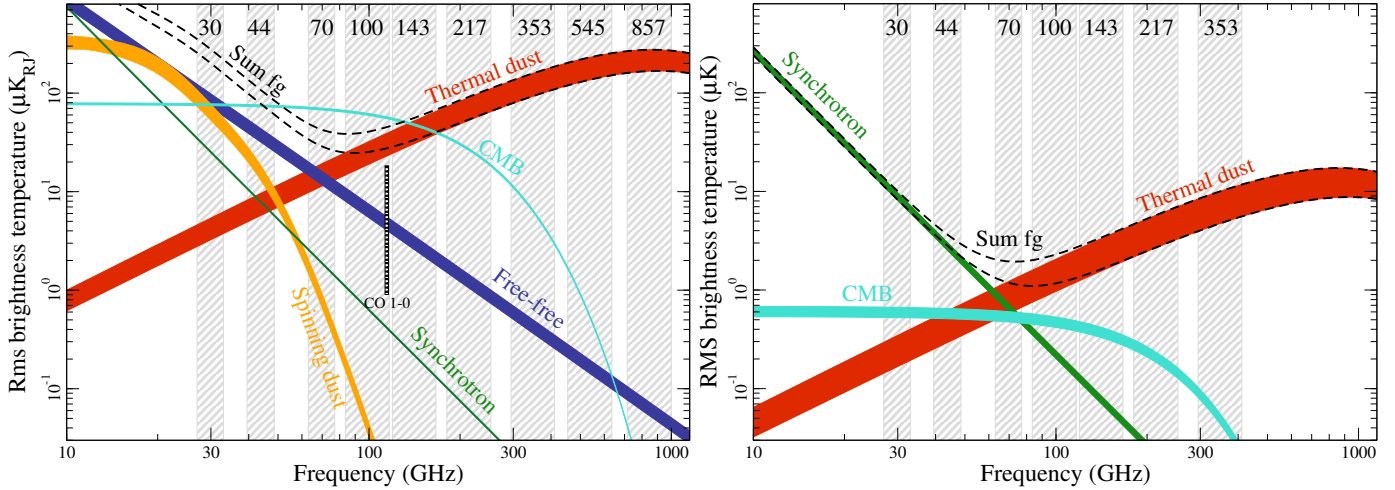
Fig. 18. Brightness temperature rms of the high-latitude sky as a function of frequency and astrophysical component for temperature (*left*) and polarization (*right*). For temperature, each component is smoothed to an angular resolution of 1° FWHM, and the lower and upper edges of each line are defined by masks covering 81 and 93% of the sky, respectively. For polarization, the corresponding smoothing scale is 40′, and the sky fractions are 73 and 93%.

Table 8. Summary of main CO product characteristics.

| Map | Algorithm | CO line | Resolution [arcmin] | Noise rms [K_{RJ} km s^{-1}] | | Analysis details | |
				15′ FWHM	60′ FWHM	Frequencies [GHz]	Model
TYPE 1	MILCA	$J = 1 \to 0$	9.6	1.4	0.34	100 (bol maps)[a]	CO, CMB
	MILCA	$J = 2 \to 1$	5.0	0.53	0.16	217 (bol maps)[a]	CO, CMB, dust
	MILCA	$J = 3 \to 2$	4.8	0.55	0.18	353 (bol maps)[a]	CO, dust
TYPE 2	MILCA	$J = 1 \to 0$	15	0.39	0.085	70, 100, 143, 353	CO, CMB, dust, free-free
	MILCA	$J = 2 \to 1$	15	0.11	0.042	70, 143, 217, 353	CO, CMB, dust, free-free
	Commander	$J = 1 \to 0$	60	$\cdots$	0.084	0.408–857	Full
	Commander	$J = 2 \to 1$	60	$\cdots$	0.037	0.408–857	Full
	Commander	$J = 3 \to 2$	60	$\cdots$	0.060	0.408–857	Full
TYPE 3	Commander	$J = 2 \to 1$[b]	7.5	0.090	0.031	143–857	CO, CMB, dust
	Commander-Ruler	$J = 1 \to 0$[c,d]	5.5	0.19	0.082	30–353	CO, CMB, dust, low-freq

Notes. [a] Built from single-bolometer maps within a given frequency (see Planck Collaboration X 2016). [b] Formally a weighted average of CO $J = 2 \to 1$ and $J = 3 \to 2$, but strongly dominated by CO $J = 2 \to 1$. [c] Formally a weighted average of CO $J = 1 \to 0$, $J = 2 \to 1$ and $J = 3 \to 2$, but strongly dominated by CO $J = 1 \to 0$. [d] Only published in 2013.

10.1. Cosmological parameters

Planck's measurements of the cosmological parameters derived from the full mission are presented and discussed in Planck Collaboration XIII (2016). As in our previous release, the data are in excellent agreement with the predictions of the 6-parameter ΛCDM model (see Table 9), with parameters tightly constrained by the angular power spectrum. The best-fit model parameters from the full mission are typically within a small fraction of a standard deviation of their values from Planck Collaboration XVI (2014), with no outliers. The constraints on the parameters of the base ΛCDM model have improved by up to a factor of 3. The largest shifts are in the scalar spectral index, n_s, which has increased by 0.7σ, and the baryon density, $\omega_b \equiv \Omega_b h^2$, which has increased by 0.6σ. Both of these shifts are partly due to correction of a systematic error that contributed to a loss of power near $\ell = 1800$ in the 2013 results (Planck Collaboration XIII 2016). This systematic also biased

the inferences on H_0 slightly low (by less than 0.5σ). In addition, the overall amplitude of the observed spectrum has shifted upwards by about 2% (in power) due to the calibration changes described in Sect. 5.4, and the optical depth to Thomson scattering, τ, has shifted down by nearly 1σ. These shifts approximately cancel in the derived normalization of the matter power spectrum. The remaining shifts are consistent with the known changes in noise level, time-stream filtering, absolute calibration, beams, and other aspects of the data processing.

Both the angular size of the sound horizon, θ_*, and the cold dark matter density, ω_c, have become significantly better determined. The data at high ℓ are now so precise, and the polarization data so constraining, that we not only see very strong evidence for three species of light neutrinos, but can measure the effective viscosity of the neutrino "fluid" to be non-zero at the 9σ level. The constraint on the baryon density, ω_b, is now comparable with the best quoted errors from big bang nucleosynthesis and suggests the possibility of calibrating nuclear capture
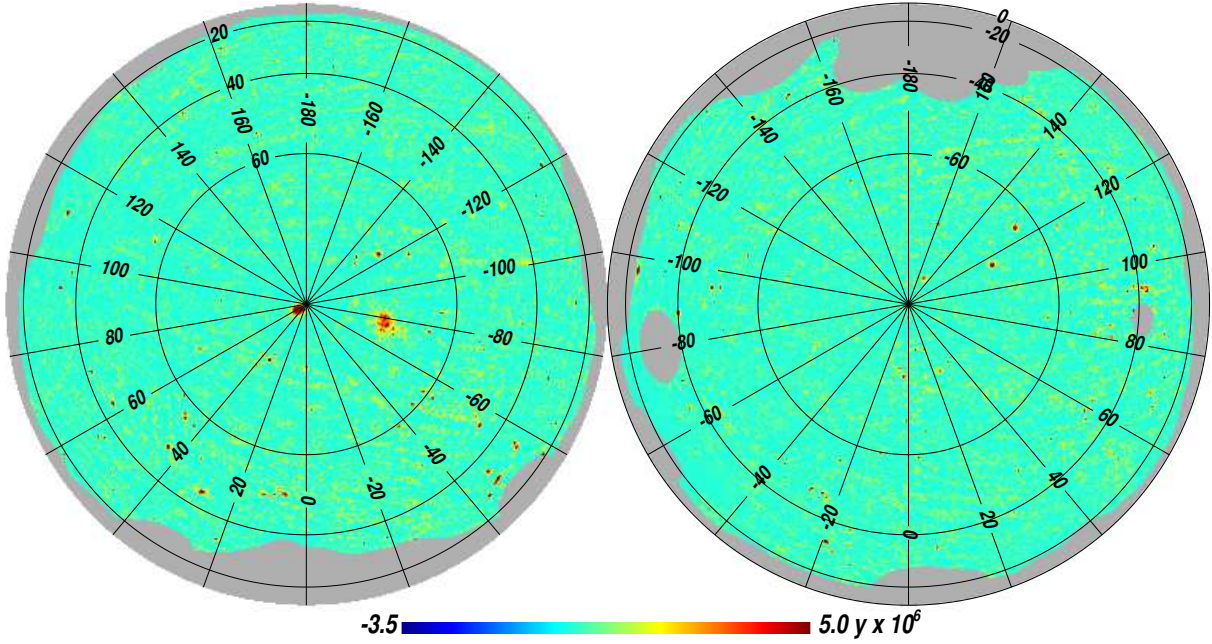
Fig. 19. Orthographic projection of the reconstructed *Planck* all-sky *y*-map in Compton parameter units ([Planck Collaboration XXII 2016](#)). For illustration purposes and to enhance the thermal SZ signal-to-noise ratio, the *y*-map has been Wiener filtered. Positive sources in the map correspond to clusters and super-clusters of galaxies with strong thermal SZ emission. In particular, the Coma and Virgo clusters are clearly visible near the north Galactic pole. The region of strongest contamination from Galactic foreground emission in the Galactic plane has been partially masked.

Table 9. Parameter best-fit values and 68% confidence levels for the base ΛCDM cosmology, computed from the *Planck* CMB power spectra, in combination with the CMB lensing likelihood ("lensing") and a compilation of external data sets ("ext").

Parameter	PlanckTT+lowP+lensing	PlanckTT, TE, EE+ lowP+lensing+ext
$\Omega_b h^2$ ...	0.02226 ± 0.00023	0.02230 ± 0.00014
$\Omega_c h^2$ ...	0.1186 ± 0.0020	0.1188 ± 0.0010
$100\theta_{MC}$.	1.04103 ± 0.00046	1.04093 ± 0.00030
τ	0.066 ± 0.016	0.066 ± 0.012
$\ln(10^{10} A_s)$	3.062 ± 0.029	3.064 ± 0.023
n_s	0.9677 ± 0.0060	0.9667 ± 0.0040
H_0	67.8 ± 0.9	67.74 ± 0.46
Ω_Λ	0.692 ± 0.012	0.6911 ± 0.0062
Ω_b	0.0484 ± 0.0010	0.04860 ± 0.00051
Ω_c	0.258 ± 0.011	0.2589 ± 0.0057
Ω_m	0.308 ± 0.012	0.3089 ± 0.0062
$\Omega_m h^2$ ...	0.1415 ± 0.0019	0.14170 ± 0.00097
$\Omega_m h^3$ ...	0.09591 ± 0.00045	0.09598 ± 0.00029
σ_8	0.815 ± 0.009	0.8159 ± 0.0086
$\sigma_8 \Omega_m^{0.5}$ ..	0.4521 ± 0.0088	0.4535 ± 0.0059
Age[Gyr]	13.799 ± 0.038	13.799 ± 0.021
r_{drag}	147.60 ± 0.43	147.50 ± 0.24
k_{eq}	0.01027 ± 0.00014	0.010288 ± 0.000071

Notes. While we see no evidence that systematics in the high-ℓ polarization are biasing parameters in the base ΛCDM model, a conservative choice would be to take the parameters listed in Col. 2.

cross-sections from CMB observations. The addition of polarization data has improved by an order of magnitude our upper limit on the annihilation rate of dark matter.

Despite trying a wide range of extensions to the basic, 6-parameter ΛCDM model, we find no significant evidence for a failure of the model. Within each extension of the parameter space, the default parameter values for the ΛCDM model remain a good fit to the data. This continues to hold when we combine the *Planck* data with other measurements, such as the distance scale measured by baryon acoustic oscillations (BAO) in galaxy surveys or Type Ia supernovae, or the growth of structure determined by redshift-space distortions. Since our best-fit cosmology has shifted by very little since our 2013 release, we continue to see tensions with some analyses of other astrophysical data sets (e.g., the abundance of clusters of galaxies, weak gravitational lensing of galaxies or cosmic shear, and distances measured by BAO in the Lyα forest at high z). [Planck Collaboration XIII](#) ([2016](#)) shows that these tensions cannot be resolved with standard single parameter extensions of the base ΛCDM model. Resolving these discrepancies remains an area of active research.

10.2. Constraints from large angular scales

The anisotropy at large angular scales, particularly the polarization, allows us to place tight constraints on the optical depth to Thomson scattering, τ, and the tensor-to-scalar ratio, r. The *Planck* temperature data, in combination with CMB lensing and low-ℓ polarization measured at 70 GHz, prefer a lower optical depth, $\tau = 0.066 \pm 0.016$, than the earlier inference from WMAP9 ($\tau \approx 0.09$, which was used in our 2013 analysis), which implies a lower redshift of reionization ($z_{re} = 8.8^{+1.7}_{-1.4}$). However, when cleaned of foregrounds using our 353 GHz channel, the WMAP polarization data are in good agreement with a lower optical depth. With the dramatic improvement in our CMB lensing detection, we are able to independently constrain τ, finding comparably tight and consistent results ($\tau = 0.071 \pm 0.016$) without the use of low-ℓ polarization. This provides additional confidence in the results.

While improved constraints on polarization at low multipoles will eventually allow us to study the reionization epoch in more detail, at present the largest impact of the change in τ comes from the implied downward shift in the inferred matter power spectrum normalization, σ_8. As it happens, much of the downward shift in this parameter is largely cancelled by the upward shift in the CMB spectrum arising from the improved calibration in the current data release.

Gravitational waves entering the horizon between recombination and today give a "tensor" contribution to the large-scale temperature and polarization anisotropies. Our strongest *Planck*-only constraint still comes from temperature anisotropies at $\ell < 10^2$ (or $k \lesssim 0.01 \ \mathrm{Mpc}^{-1}$), and is thus limited by cosmic variance and is model-dependent. Tensor modes also generate a *B*-mode signal, which peaks at $\ell \approx 10^2$, slightly smaller scales than the bulk of the temperature signal. The cosmological landscape became more complicated in early 2014 with the detection of *B*-mode polarization anisotropy by the BICEP2 team (BICEP2 Collaboration 2014). Analysis of *Planck* polarization data at high Galactic latitudes demonstrated that no region of the sky can be considered dust-free when searching for primordial *B*-modes (Planck Collaboration Int. XXX 2016), and a joint analysis of BICEP2/Keck Array observations and *Planck* polarization data (BICEP2/Keck Array and Planck Collaborations 2015) shows that polarized dust emission contributes a significant part of the BICEP2 signal. Combining the *Planck* and revised BICEP2/Keck Array likelihoods leads to a 95% upper limit of $r_{0.002} < 0.09$. This eliminates any tension between the BICEP2 and *Planck* results, and in combination with our other constraints disfavours inflationary models with a ϕ^2 potential. This and other implications for inflationary models in the early Universe are discussed more fully in Planck Collaboration XIII (2016) and Planck Collaboration XX (2016).

10.3. Dark energy and modified gravity

Even though much of the weight in the *Planck* data lies at high redshift, *Planck* can still provide tight constraints on dark energy and modified gravity models, especially when used in combination with other probes. This is explored in Planck Collaboration XIV (2016), which focuses on tests of dark energy and modified gravity on the scales where linear theory is most applicable, since these are the most theoretically robust. As for Planck Collaboration XIII (2016), the results are consistent with the simplest scenario, ΛCDM, though all constraints on dark energy models (including minimally-coupled scalar field models or evolving equation of state models) and modified gravity models (including effective field theory, phenomenological, $f(R)$, and coupled dark energy models) are considerably improved with respect to past analyses. In particular, we improve significantly the constraint on the density of dark energy at early times, finding that it has to be below 2% (95% confidence) of the critical density, even if it only plays a role at $z < 50$. Constraints are tighter if early dark energy is present since recombination, with $\Omega_e < 0.0071$ (for the data combination PlanckTT+lensing+BAO+SNe+H_0), and an even tighter bound results if high-ℓ polarization is included. In models where perturbations are modified, even if the background is ΛCDM, a few tensions appear, mainly driven by external data sets.

10.4. Lensing of the CMB

The CMB fluctuations measured by *Planck* provide a slightly perturbed image of the last-scattering surface, due to the effects of gravitational lensing by large-scale structure. Lensing slightly washes out the acoustic peaks of the CMB power spectrum, an effect we see in the *Planck* data at high significance. Lensing also introduces distinctive non-Gaussian features into the CMB maps, which allow us to map and make statistical measurements of the gravitational potentials, and the associated matter. These are studied in detail in Planck Collaboration XV (2016). The lensing signal is consistent with the basic, 6-parameter, ΛCDM model that best fits the temperature data. This gives us a very strong consistency check on the gravitational instability paradigm and the growth of structure over more than two decades in expansion factor.

Since it provides sensitivity to the growth of structure between the surface of last scattering and the present epoch, the lensing signal allows us to measure a number of important parameters by breaking parameter degeneracies. Figure 20 shows the lensing power spectrum, which for the first time is measured with higher accuracy than it is predicted by the base ΛCDM model that fits the temperature data. With the temperature-only nominal mission data from the 2013 *Planck* data release, we were able to make the most powerful measurement of lensing to that date (at a level of 25σ). In the current release, incorporating additional temperature data, as well as entirely new polarization information, we have nearly doubled the power of this measurement to 40σ. This is the most significant detection to date, allowing lensing to be used as part of our precision cosmology suite.

10.5. Inflation

The release of the 2013 *Planck* data and findings had an enormous impact on the inflationary community, and the *Planck* 2015 results continue to demonstrate the importance of this window into the early Universe. Planck Collaboration XX (2016) presents our constraints on inflationary models. The *Planck* data are consistent with a purely adiabatic, power-law spectrum of initial fluctuations, whose spectral index ($n_s = 0.9677 \pm 0.006$) is significantly different from unity. The addition of polarization data has significantly improved the limits on any isocurvature modes, which are now constrained at the percent level. Despite a detailed search, and study of several models, we see no statistically significant evidence for departures from a power law. The combination of *Planck* data with the BICEP2/Keck Array data provide a strong upper limit on the tensor-to-scalar ratio, and disfavour all monomial models ($V(\phi) \propto \phi^{2p}$) with $p \geq 1$. This is an important milestone, since these form the simplest class of inflationary models.

10.6. Primordial non-Gaussianity

Planck Collaboration XVII (2016) for the first time uses polarization information to constrain non-Gaussian signals left by primordial physics. The results significantly reduce the allowed model space spanned by local, equilateral, and orthogonal non-Gaussianity, tightening constraints by up to 45%. In particular, $f_{\mathrm{NL}}^{\mathrm{local}} = 0.8 \pm 5.0$, $f_{\mathrm{NL}}^{\mathrm{equil}} = -4 \pm 43$, and $f_{\mathrm{NL}}^{\mathrm{ortho}} = -26 \pm 21$. In addition, the *Planck* 2015 analysis covers a greatly extended range of primordial 3-point and 4-point signals, constraining inflationary model space as well as some proposed alternatives to inflation. The global picture that emerges is one of consistency
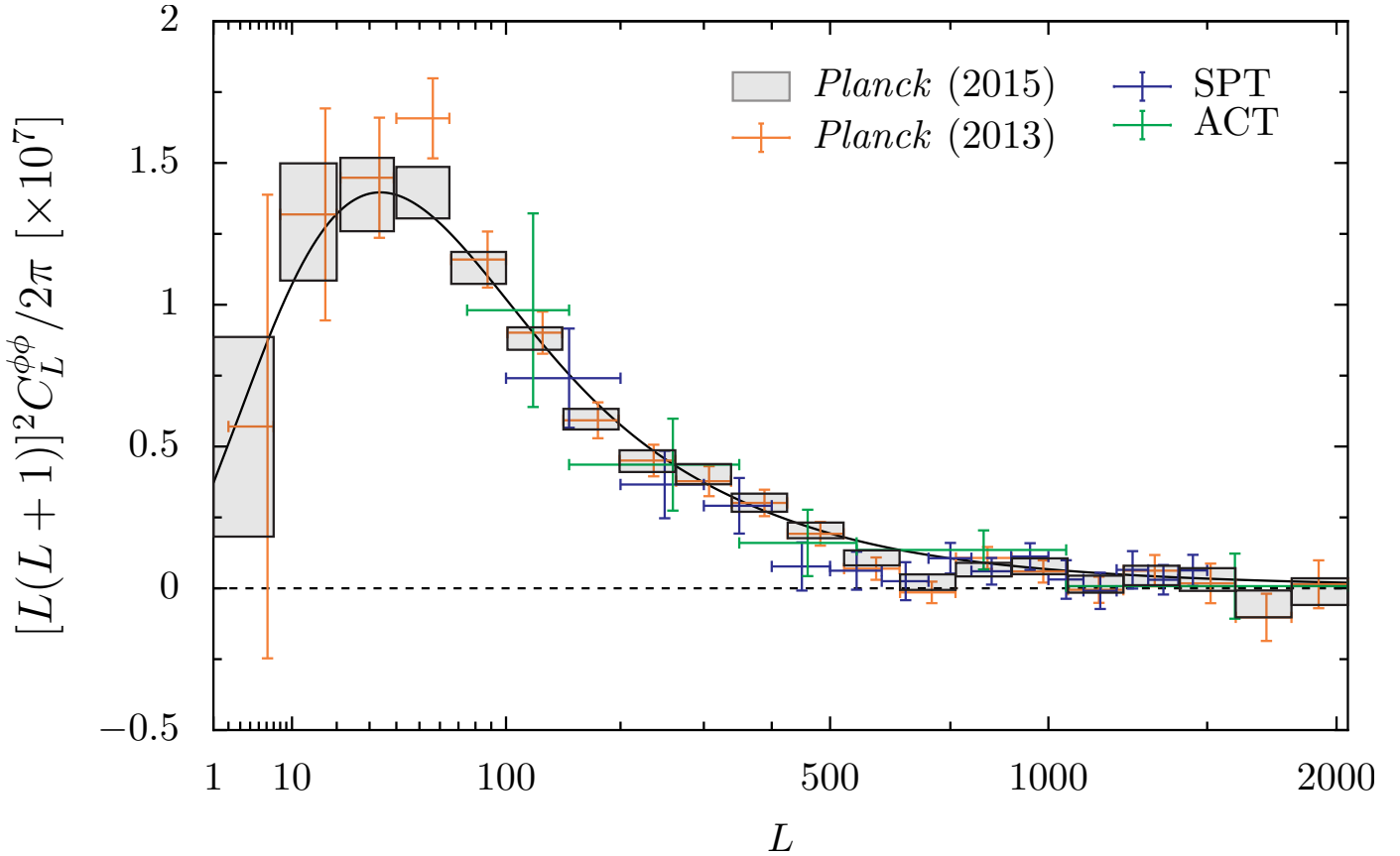
Fig. 20. Lensing potential power spectrum estimate from the 2015 data release (Planck Collaboration XV 2016), based on the SMICA CMB map, as well as previous reconstructions from *Planck* and other experiments for comparison.

with the premises of ΛCDM cosmology, namely that the structure we observe today is the consequence of the passive evolution of adiabatic, Gaussian, nearly scale-invariant, primordial seed perturbations.

10.7. Isotropy and statistics

The *Planck* 2013 results determined the presence of statistically anisotropic signals in the CMB, confirming previous studies made using WMAP data. Such anomalies therefore constitute real features of the microwave sky, and potentially challenge fundamental assumptions of the standard cosmological model. Planck Collaboration XVI (2016) extends these studies based mainly on the full *Planck* mission for temperature, but also including some polarization measurements. A large number of statistical tests indicate consistency with Gaussianity, while a power deficit at large angular scales is manifested in several ways, for example in low map variance. The well-known "Cold Spot" is identified through various methods. Tests of directionality suggest the presence of angular clustering from large to small scales, but at a significance that is dependent on the details of the approach. On large angular scales, a dipolar power asymmetry is investigated through several approaches, and we address the subject of a posteriori correction. Our ability to include results based on polarization data is limited by two factors. First, CMB polarization maps have been high-pass filtered to mitigate residual large-scale systematic errors in the HFI channels, thus eliminating structure in the maps on angular scales larger than about 10°. Second, an observed noise mismatch between the simulations and the data precludes robust conclusions based on the

null-hypothesis approach adopted throughout the paper. Nevertheless, we perform the first examination of polarization data via a stacking analysis, in which the stacking of the data themselves necessarily acts to lower the effect of the noise mismatch. We find that the morphology of the stacked peaks is consistent with the expectations of statistically isotropic simulations. Further studies of the large angular scale structure of the CMB polarization anisotropy will be conducted with data of improved quality expected to be released in 2016.

10.8. The ISW effect

The 2013 results on the integrated Sachs-Wolfe (ISW, Planck Collaboration XIX 2014) effect have been refined and extended using the full mission data (Planck Collaboration XXI 2016). We now detect the ISW effect at 4σ by cross-correlating the *Planck* CMB temperature map with tracers of the large-scale structure, in particular: the NRAO VLA Sky Survey (NVSS) radio catalogue; the photometric luminous galaxy catalogue from the Baryonic Oscillation Spectroscopic Survey of the Sloan Digital Sky Survey (SDSS) III; the photometrically-selected galaxies from the SDSS-DR8 catalogue; the Wide-field Infrared Survey Explorer (WISE) galaxy and AGN catalogues; and the *Planck* lensing map. The ISW-lensing bispectrum (Planck Collaboration XIX 2014; Planck Collaboration XXII 2014; Planck Collaboration XXVI 2014) gives a detection at approximately 3σ, 20% higher than the level achieved with the 2013 release. The increase is due to the lower noise in the full mission temperature data, and to the

addition of polarization data, which enter into the ISW detection levels mentioned above through the *Planck* lensing map.

Since a purely gravitational effect does not polarize photons, polarization data in principle provide a powerful discriminant between ISW and primary CMB fluctuations. The current *Planck* polarization maps, however, are not usable at the largest scales (Sect. 2.2), so this tool cannot yet be fully exploited.

Polarization data on smaller scales ($\gtrsim 5°$) can be used to probe the ISW effect through stacking of CMB anisotropies at the positions of known superstructures. We have studied the photometric profiles of *Planck* CMB polarization patches at the locations of the Granett et al. (2008) catalogue of superclusters and super-voids, which have been reported as anomalous ISW sources (e.g., Planck Collaboration XVII 2014). Our analysis, using specially-constructed CMB temperature maps that are correlated and uncorrelated with *E*-modes, cannot rule out the ISW effect as the cause of these anomalies.

A map of the ISW anisotropies is presented in Fig. 21. It shows the redshifts and blueshifts suffered by CMB photons travelling through the gravitational potential traced by different galaxy catalogues and the *Planck* lensing map. Our reconstruction has a mean error of $\approx 15~\mu$K (per roughly 1° pixel).

10.9. Cosmology from clusters

In 2013 we found an apparent tension between our primary CMB constraints and those from the *Planck* cluster counts, with the clusters preferring a lower normalization of the matter power spectrum, σ_8. The comparison is interesting because the cluster counts directly measure σ_8 at low redshift and hence any tension could signal the need for extensions of the base model, such as non-minimal neutrino mass. However, limited knowledge of the normalization of the scaling relation between SZ signal and mass (usually called "mass bias") continues to hamper the interpretation of this result.

Our 2015 cluster analysis benefits from a larger catalogue (438 objects versus the 189 in 2013), greater control of the selection function, and recent gravitational lensing determinations of the mass bias for *Planck* clusters. With the larger sample, we now fit the counts in the 2-dimensional plane of redshift and S/N, allowing us to simultaneously constrain the slope of the scaling relation and the cosmological parameters. We examine three new empirical determinations of the mass bias from gravitational lensing: weighing the Giants (WtG; von der Linden et al. 2014); the Canadian Cluster Comparison Project (CCCP; Hoekstra et al., priv. comm.); and results from a new method based on CMB lensing (Melin & Bartlett 2015). We use these three results as priors because they measure the mass scale directly on samples of *Planck* clusters.

The cluster constraints on σ_8 and Ω_m are statistically identical to those of 2013 when adopting the same scaling relation and mass bias; in this sense, we confirm the 2013 results with the larger 2015 catalogue. Applying the three new mass bias priors, we find that the WtG calibration reduces the tension with the primary CMB constraints to slightly more than 1σ in the base model, and CCCP results in tension at just over 2σ, similar to the case for the CMB lensing calibration. More detailed discussion of constraints from *Planck* cluster counts can be found in Planck Collaboration XXIV (2016).

11. *Planck* 2015 astrophysics results

11.1. Low frequency foregrounds

Galactic foreground emission between 20 and 100 GHz, based primarily on the `Commander` component separation of Planck Collaboration X (2016), is discussed in Planck Collaboration XXV (2016). The total intensity in this part of the spectrum is dominated by free-free and spinning dust emission, while polarization is dominated by synchrotron emission.

Comparison with radio recombination line templates verifies the recovery of the free-free emission along the Galactic plane. Comparison of high-latitude Hα emission with our free-free map shows residuals that correlate with dust optical depth, consistent with a fraction (around 30%) of Hα having been scattered by high-latitude dust. A number of diffuse morphological features of spinning dust at high latitude can be highlighted. There is substantial spatial variation in the spinning dust spectrum, with the emission peak (in I_ν) ranging from below 20 GHz to more than 50 GHz. There is a strong tendency for the spinning dust component near prominent H II regions to have a higher peak frequency, suggesting that this increase in peak frequency is associated with dust in the photo-dissociation regions around the nebulae. The emissivity of spinning dust in these diffuse regions is of the same order as previous detections in the literature. Over the entire sky, the `Commander` solution finds more anomalous microwave emission (AME) than the WMAP component maps, at the expense of synchrotron and free-free emission. Although the `Commander` model fits the data exceptionally well, as noted in Sect 9.4, the discrepancy is largely driven by differences in the assumed synchrotron spectrum and the more elaborate model of spinning dust designed to allow for the variation in peak frequency noted above. Future surveys, particularly at 5–20 GHz, will greatly improve the separation, since the predicted brightness between the two models disagrees substantially in that range.

In polarization, synchrotron emission completely dominates on angular scales larger than 1° and frequencies up to 44 GHz. We combine *Planck* and WMAP data to make the highest signal-to-noise ratio map yet of the intensity of the all-sky polarized synchrotron emission at frequencies above a few gigahertz, where Faraday rotation and depolarization are negligible (Figs. 22 and 23). Most of the high-latitude polarized emission is associated with distinct large-scale loops and spurs, and we rediscuss their structure following the earlier study of Vidal et al. (2015) based on WMAP observations. We argue that nearly all the emission at $-90° < l < 40°$ is part of the Loop I structure, and show that the emission extends much further into the southern Galactic hemisphere than previously recognized, giving Loop I an ovoid rather than circular outline. However, it does not continue as far as the "*Fermi* bubble/microwave haze", which probably rules out an association between the two structures. The South Polar Spur (SPS, see Fig. 22) is bordered by a polarized dust filament and associated low-velocity H I emission, analogous to the cold features long known to border Loop I around the North Polar Spur. We find two structures that could correspond to distant analogues of the radio loops, as predicted by Mertsch & Sarkar (2013), including one surrounding the Cygnus X star-forming region, both of which are again associated with dust polarization.

We identify a number of other faint features in the polarized sky, including a dearth of polarized synchrotron emission directly correlated with a narrow, 20°-long filament seen in Hα at high Galactic latitude, and also visible in the Faraday rotation map of Oppermann et al. (2012). Finally, we look for evidence of